Supporting Information

Accelerated Lithium-ion Conduction in Covalent Organic Frameworks

Li Sheng, Li Wang, Jianlong Wang, Hong Xu, Xiangming He**

Institute of Nuclear and New Energy Technology, Tsinghua University, Beijing 100084, China

**E-mail: hongxu@tsinghua.edu.cn, hexm@tsinghua.edu.cn*

Table of Contents

A. Materials and methods........................2
B. DFT calculated charge distribution of TPB-DMTP-COF channel and dissociation of $Li(EC)_4^+$ in different environment........................4
C. XRD measurement of TPB-DMTP-COF and DFT-calculated crystalline structure........................7
D. Thermal stability........................10
E. Impedance measurement........................11
F. SEM image of complex Celgard+TPB-DMTP-COF membrane and conductivity comparison of reported separators........................14
G. Transference Number Measurements........................16
H. Electrochemical stability........................20
I. References........................21

A. Materials and methods

Materials

1,3,5-Tri-(4-aminophenyl)benzene (TAPB), 2,5-dimethoxyterephthalaldehyde (DMTA) were obtained from TCI. Acetic acid, 1,2-Dichlorobenzene (*o*-DCB) was obtained from ACROS organics, tetrahydrofuran (THF), and *n*-Butanol (BuOH) were obtained from Xilong Chemicals. PVDF powder with the average Mw around 534,000 was purchased from Aldrich.

The microporous polyolefin separator Celgard 2400 was provided by Celgard Inc.; the liquid electrolyte was manufactured by Beijing Institute of Chemical Reagents Co., Ltd. The electrolyte used was 1 M solution of $LiPF_6$ in a 1/1/1 (v/v/v) mixture of ethylene carbonate (EC), dimethyl carbonate (DMC) and ethyl methyl carbonate (EMC). The electrolyte was stored in argon-filled glove box, the oxygen and water contents were controlled to below 0.2 ppm.

Synthesize of TPB-DMTP-COF. An *o*-dichlorobenzene (*o*-DCB)/*n*-BuOH (0.5/0.5 ml) mixture of 1,3,5-tri-(4-aminophenyl)benzene (TAPB) (0.08 mmol, 28.1 mg) and 2,5-dimethoxyterephthalaldehyde (DMTA) (0.12 mmol, 23.3 mg) in the presence of an acetic-acid catalyst (6 M, 0.1 ml) in a Pyrex tube (10 ml) was degassed via three freeze-pump-thaw cycles. The tube was flame sealed and heated at 120 ℃ for three days. The precipitate was collected via centrifugation, washed several times with THF and then subjected to Soxhlet extraction with THF as the solvent for one day to remove the trapped guest molecules. The yellow powder was collected and dried at 120 ℃ under vacuum overnight to produce TPB-DMTP-COF in an isolated yield of 80%.

Materials Characterizations

Powder X-ray diffraction (PXRD) data were recorded on a D8 Advance Brooker Ultima III diffractometer by depositing powder on glass substrate, from $2\theta = 1.0°$ up to 30° at 1°/min increment. Nitrogen sorption isotherms were measured at 77 K with a Quantachrome IQ2 Instrument Corporation model 3Flex surface characterization analyzer. Thermogravimetric analysis (TGA) was performed on a TA instrument Q5000IR TGA under Nitrogen by heating to 600 ^{o}C at a heating rate of 10 ^{o}C min^{-1}. High-resolution transmission electron microscopy (HR-TEM) images were obtained on a JEOL model JEM-2010 microscopy. The sample was prepared by drop-casting a supersonicated tetrahydrofuran suspension of the COF onto a copper grid. The Brunauer Emmett-Teller (BET) method was utilized to calculate the specific surface areas. By using the quenched solid density functional theory (QSDFT) model,[1-2] the pore size distribution was derived from the sorption curve. The microscopic morphologies of the samples were characterized by field emission scanning electron microscopy (ZEISS Gemini, 5 kV, Germany).

Computational Calculations

The electrolyte accommodated COF can be viewed as a host-guest adsorption system, which is ubiquitous in the field of porous materials and surface chemistry. Thus, we employ a molecular forcefield based method to construct the initial configuration of the electrolyte adsorption model. 1×1×5 lattices (5 repeating layers with a distance of 18.71 Å) of TPB-DMTP-COF was chosen as host to adsorb 5 representative electrolyte components: $Li(EC)_4^+$, PF_6^-, EC, DMC, and EMC (EC: ethylene carbonate, DMC: dimethyl carbonate, EMC: ethyl methyl carbonate). Metropolis Monte Carlo method[3] was utilized for possible adsorption configuration searching and COMPASS II force field[4-6] was used for calculating charges and non-bond interactions; simulation was implemented in the Adsorption Locator modules of Materials Studio. To avoid the influence of the less accurate molecular force field to the initial geometry, both the host framework and the guest molecules are kept rigid during the adsorption process. The obtained low energy adsorption configurations are then optimized by means of DFT method using CASTEP code,[7] with GGA-PBE[8] as functional, Grimme dispersion correction[9-10] for van der Waals (vdW) and π-stacking interactions describing.

All simulation works were performed using the computing resources at National Supercomputing Center in Shenzhen.

B. DFT calculated charge distribution of TPB-DMTP-COF channel and dissociation of $Li(EC)_4^+$ in different environment.

Hexagonal structure of TPB-DMTP-COF.

The ordered, one-dimensional nanochannel feature of TPB-DMTP-COF (Fig. S1) provides a good platform to investigate surface-dependent conductivity and cation/anion transport preference.

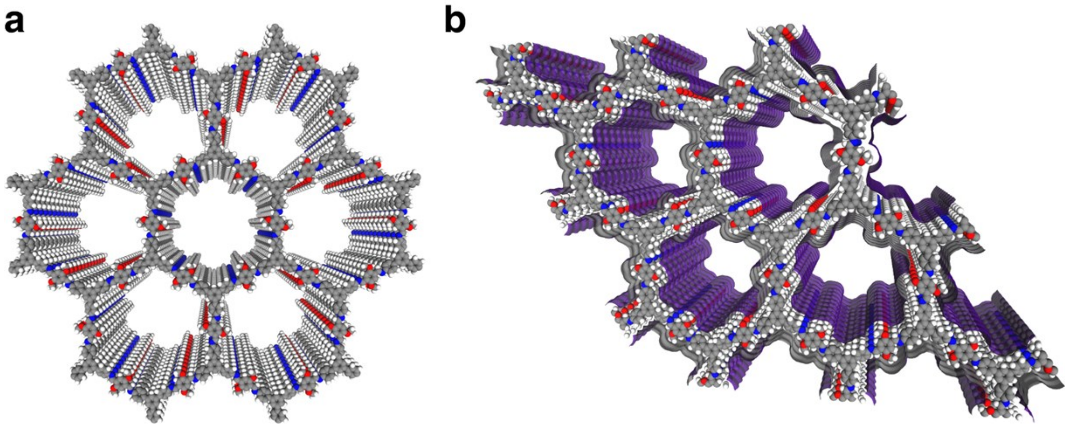

Fig. S1 (a) Ordered 1D open channels. (b) Accessible surface of TPB-DMTP-COF (in purple). (red, O; blue, N; grey, C; white, H).

DFT-calculated surface charge distribution of TPB-DMTP-COF.

The surface charge distribution of the host-guest complex under the environment of electrolyte was investigated (Fig. S2). The CASTEP optimized structures were then calculated with implicit solvent model using DFT-COSMO (density functional theory based conductor-like screening model) method[11-14]. DFT-COSMO calculations were performed using DMol3 module[15-16] of Materials Studio. Double Numerical basis with Polarization functions (DNP) was selected as the basis set; GGA-PBE[8] was selected as the exchange-correlation functional. Grimme dispersion correction[9-10] was employed in all calculations to describe van der Waals (vdW) and π-stacking interactions.

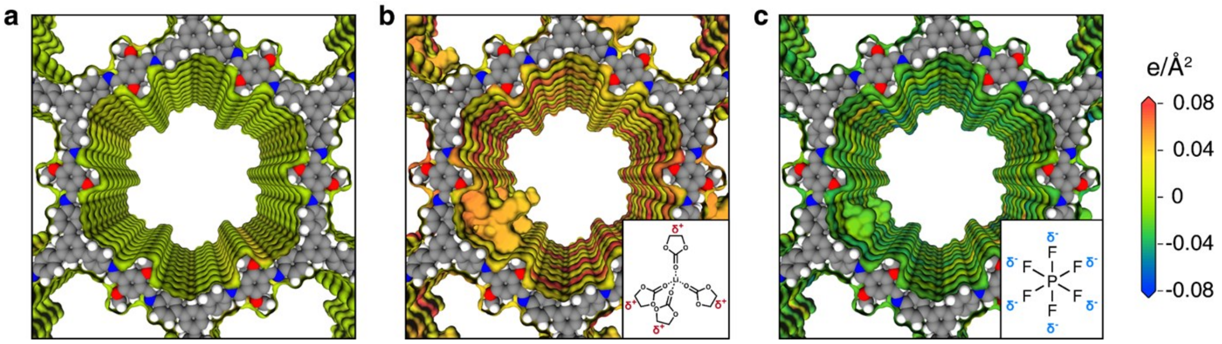

Figure S2. DFT calculated charge distribution of TPB-DMTP-COF channel walls. (a) Pristine TPB-DMTP-COF. (b) After adsorption of $Li(EC)_4^+$, inset shows the chemical structure of $Li(EC)_4^+$. (c) After adsorption of PF_6^-, inset shows the chemical structure of PF_6^-. (red, O; blue, N; grey, C; white, H).

DFT-calculated dissociation energy of $Li(EC)_4^+$ in different environment.

The DFT-calculated adsorption energy of different molecules of liquid electrolyte(Table S1). The absorption energy ($\mathbf{E_{adsorp.}}$) was calculated as $\mathbf{E_{adsorp.}} = \mathbf{E_{(COF\text{-}adsorbates)}}\text{-}\mathbf{E_{(COF)}}\text{-}\mathbf{E_{(adsorbates)}}$, where the $\mathbf{E_{COF}}$, $\mathbf{E_{adsorbates}}$ and $\mathbf{E_{COF\text{-}adsorbates}}$ are the energy of TPB-DMTP-COF, adsorbates and adsorbate-loaded COF. The desolvation energy ($\mathbf{E_{desol\text{-}COF}}$) of $Li(EC)_4^+$ on the surface of COF was calculated as $\mathbf{E_{desol\text{-}COF}} = \mathbf{E_{(COF\text{-}Li(EC)3)}}+\mathbf{E_{(EC)}}\text{-}\mathbf{E_{(Li(EC)4)}}\text{-}\mathbf{E_{(pristine\text{-}COF)}}$, the corresponding DFT calculation model was shown in Fig. S3. The dissociation energy of $Li(EC)_4^+$ to $Li(EC)_3^+$ and EC molecule is calculated to be 45.27 kJ mol^{-1} in the pure liquid electrolyte, while much lower desolvation energy of 21.67 kJ mol^{-1} in the channels of TPB-DMTP-COF (Fig. S4).

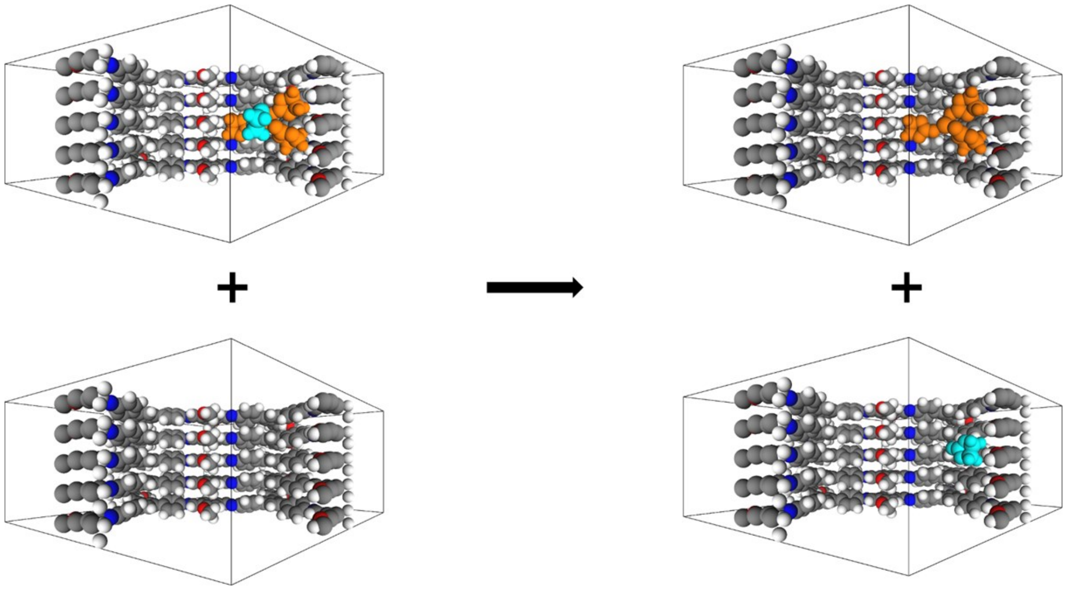

Fig. S3 DFT calculation model of $Li(EC)_4^+$ desolvation on the channel walls of COF. (red, O; blue, N; grey, C; white, H; the desolvation fragments were highlighted for clarity: $Li(EC)_3^+$, orange; EC: cyan

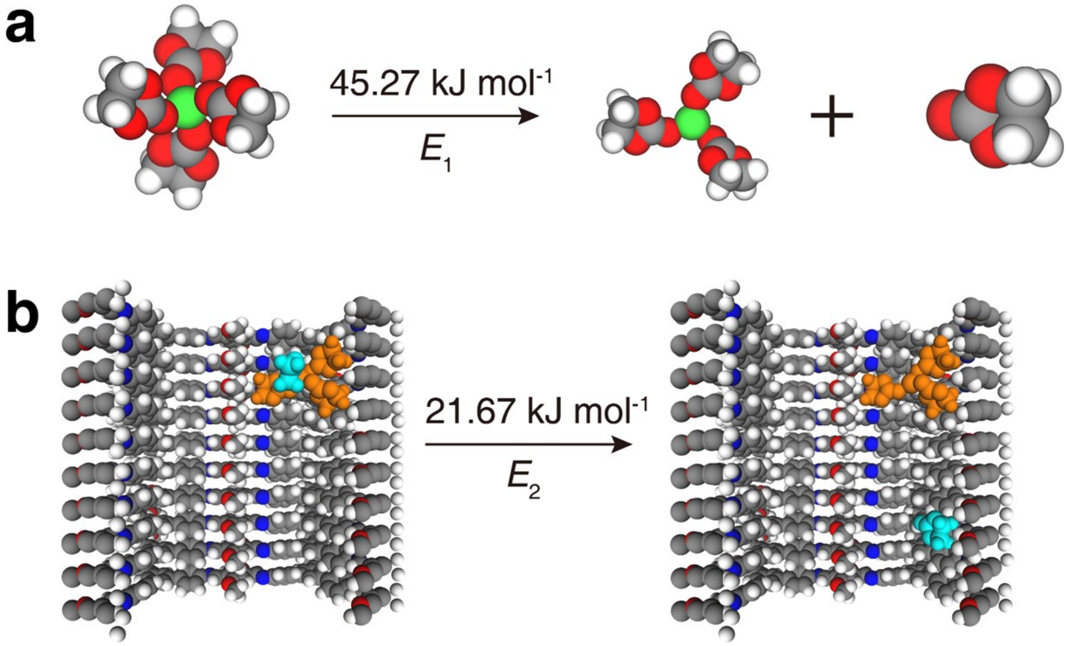

Fig. S4 (a) In the pure liquid electrolyte. (b) On the channel wall of TPB-DMTP-COF.

Table S1. DFT-calculated adsorption energy of different guest molecules: ethylene carbonate (EC), dimethyl carbonate (DMC), ethyl methyl carbonate (EMC) and PF_6^- on TPB-DMTP-COF surfaces (COF for short in this Table).

Adsorption Energy	COF-EC	COF-DMC	COF-EMC	COF-PF_6^-	COF-$Li(EC)_4^+$
kJ mol^{-1}	-24.5	-21.2	-34.5	-347.7	-497.5

C. XRD measurement of TPB-DMTP-COF and DFT-calculated crystalline structure.

The crystalline structure of TPB-DMTP-COF was determined using the density functional theory (DFT)[17-18] implemented in the CASTEP[7] module of Materials Studio. The generalized gradient approximation in the form of Perdew–Burke–Ernzerhof (PBE)[8] was selected as the exchange-correlation functional. Grimme dispersion correction[9-10] was employed in all calculations to describe van der Waals (vdW) and π-stacking interactions. A plane wave energy cutoff of 830 eV and the Monkhorst-Pack k-point grid of $1\times1\times4$ were used. The lattice dimensions were optimized simultaneously with the geometry. The convergence criteria for energy, force, stress and displacement are 5×10^{-6} eV/atom, 0.01 eV/Å, 0.02 GPa and 5×10^{-4} Å, respectively. The optimized TPB-DMTP-COF possesses a space group of $P6$ with $a = b$ =37.2322 Å, interlayer distance (c) of 3.7421 Å, $\alpha = \beta = 90^\circ$ and $\gamma = 120^\circ$ (Fig. S5, Table S2).

The powder X-ray diffraction (PXRD) pattern simulation was performed using a software package for crystal determination from PXRD pattern, implemented in Reflex module of Materials Studio. We performed Pawley refinement to optimize the lattice parameters iteratively until the R_P and R_{WP} values converge. The pseudo-Voigt profile function was used for whole profile fitting and Finger-Cox-Jephcoat function[19] was used for asymmetry correction during the refinement processes. The DFT calculated crystalline structure resulted in a simulated PXRD pattern (Fig. S5c, black curve) that was consistent with the experimentally observed curve. Pawley refinement (Fig. S5c, blue curve) also confirmed a good match of calculated and observed PXRD pattern (Fig. S5c, red curve), as evidenced by the negligible difference (Fig. S5c, green curve). The Pawley refinement leads to a space group of $P6$ with $a = b$ =37.2814 Å, c = 3.7596 Å, $\alpha = \beta = 90^\circ$ and $\gamma = 120^\circ$, and R_p and R_{wp} values of 3.97% and 6.51%, respectively (Table S3).

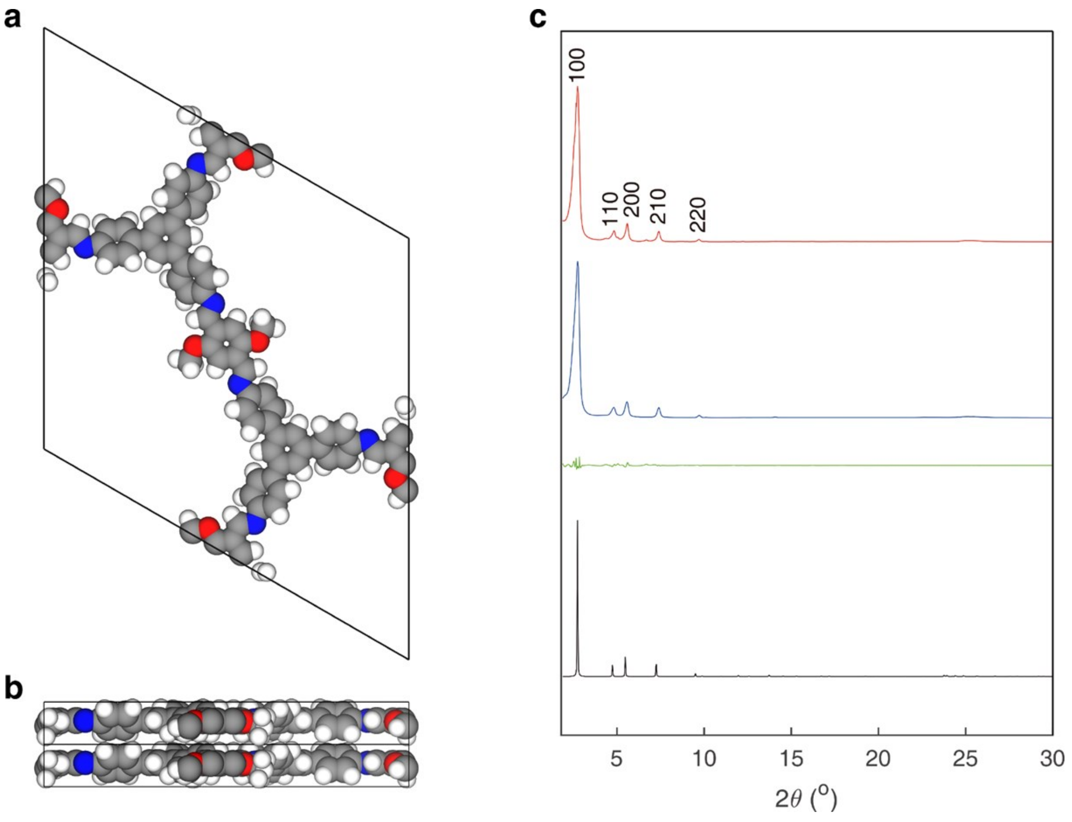

Fig. S5 Crystal structure and X-ray diffraction of TPB-DMTP-COF. Unit cell of TPB-DMTP-COF, (a) top view; (b) side view. (c) PXRD patterns of TPB-DMTP-COF (red curve), the Pawley refinement result (blue curve) and their difference (green curve), the calculated result (black curve).

Table S2. Atomistic coordinates of TPB-DMTP-COF optimized by using DFT method in CASTEP with PBE as functional.

Space group: *P6;*

$a = b = 37.2322$ Å, $c = 3.7421$ Å;

$\alpha = \beta = 90^\circ$, $\gamma = 120^\circ$.

Atom	x/a	y/b	z/c
C	0.28965	0.64139	0.56708
C	0.31521	0.62367	0.56722
C	0.244	0.61502	0.56516
C	0.37132	0.59011	0.40311
C	0.39592	0.57177	0.39929
C	0.43561	0.5919	0.55796
C	0.44986	0.63123	0.71215
C	0.42483	0.64907	0.71928
N	0.46266	0.57582	0.56151
C	0.44739	0.53592	0.56227
C	0.47396	0.5176	0.5528
C	0.45674	0.4739	0.54692
C	0.48265	0.45701	0.54867
O	0.41424	0.45022	0.53839
C	0.60249	0.59198	0.43441
H	0.30104	0.59001	0.56635

H	0.34163	0.57498	0.2637
H	0.38538	0.54263	0.25696
H	0.48041	0.64658	0.8368
H	0.43579	0.67864	0.85545
H	0.41378	0.51416	0.57638
H	0.47061	0.42368	0.54728
H	0.58817	0.59401	0.18335
H	0.63583	0.60429	0.39652
H	0.59754	0.61021	0.64102

Table S3. Atomistic coordinates for the refined unit cell parameters for TPB-DMTP-COF via Pawley refinement.

Space group: *P6;*

$a = b = 37.2814$ Å, $c = 3.7596$ Å;

$\alpha = \beta = 90^\circ$, $\gamma = 120^\circ$.

Atom	x/a	y/b	z/c
C	0.28965	0.64139	0.56708
C	0.31521	0.62367	0.56722
C	0.244	0.61502	0.56516
C	0.37132	0.59011	0.40311
C	0.39592	0.57177	0.39929
C	0.43561	0.5919	0.55796
C	0.44986	0.63123	0.71215
C	0.42483	0.64907	0.71928
N	0.46266	0.57582	0.56151
C	0.44739	0.53592	0.56227
C	0.47396	0.5176	0.5528
C	0.45674	0.4739	0.54692
C	0.48265	0.45701	0.54867
O	0.41424	0.45022	0.53839
C	0.60249	0.59198	0.43441
H	0.30104	0.59001	0.56635
H	0.34163	0.57498	0.2637
H	0.38538	0.54263	0.25696
H	0.48041	0.64658	0.8368
H	0.43579	0.67864	0.85545
H	0.41378	0.51416	0.57638
H	0.47061	0.42368	0.54728
H	0.58817	0.59401	0.18335
H	0.63583	0.60429	0.39652
H	0.59754	0.61021	0.64102

D. Thermal stability

The thermal stabilities of the TPB-DMTP-COF and Celgard2400 were evaluated by TGA in nitrogen. As shown in Fig. S6, the COF has higher thermal stability than that of the Celgard, which well meets the requirement for use in the lithium-ion battery.

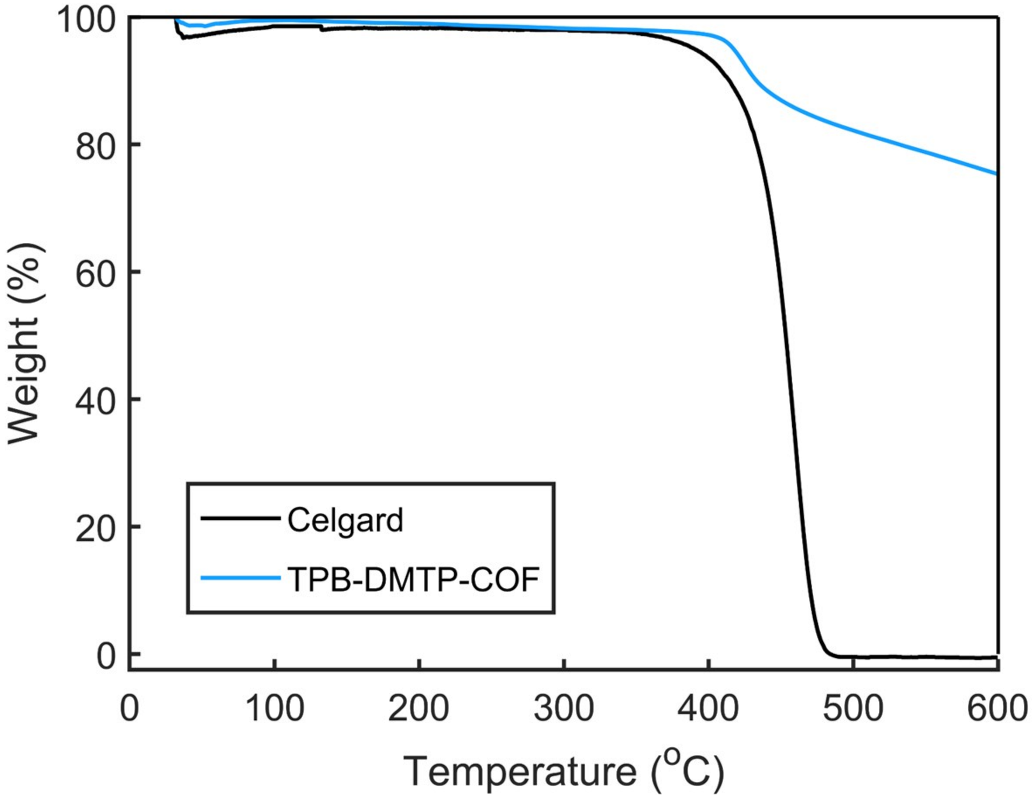

Fig. S6 Thermal stability of Celgard and TPB-DMTP-COF. TGA curves of the Celgard (black) and TPB-DMTP-COF (blue) in nitrogen.

E. Impedance measurement

Photos of TPB-DMTP-COF pellets at different conditions

The COF pellets were prepared by mixing the COF powers with PVDF in a 9:1 weight ratio, then, the mixture was milled in a mortar with 2 wt% of N-Methyl-2-pyrrolidone (NMP). Then the mixture was added into a 13-mm standard die, and slowly increased pressure to 20 MPa, keep for 10 min at room temperature to prepare pellets, the thickness of which is around 0.361-0.377 mm, the density is 0.63 g cm^{-3}. 1 g TPB-DMTP-COF pellet could adsorb 1.1 g liquid electrolyte (immersed the pellet into the liquid electrolyte for 5 h, and the COF pellet became dark after absorbed liquid electrolyte (Fig. S7a and 7b). The pellet remained good mechanical and did not show any cracks or fragments on repetitive use (Fig. S7c).

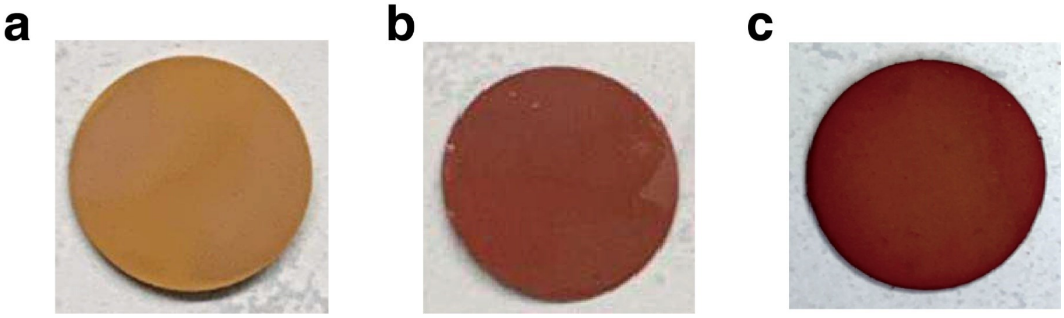

Fig. S7 Photos of TPB-DMTP-COF pellets at different conditions. (a) The pressed TPB-DMTP-COF pellet. (b) After absorbed with liquid electrolyte (1.0 M LiPF$_6$ in EC/DMC/EMC (1/1/1, by volume)). (c) After impedance measurement.

Impedance measurement

Impedance analyses were performed on electrolyte-filled COF in a stainless-steel symmetric cell, which was assembled in an argon-filled glove box. Measurements were performed on a CHI660E Electrochemical Workstation (Shanghai Chenhua) with electrochemical impedance spectroscopy (EIS), with the frequency range from 0.1 Hz to 10 KHz and with a perturbation amplitude of 5 mV, over a temperature range of 20 to 60 ^{o}C. The cells were equilibrated in an oven, and at each set temperature was left standing for 30 min before EIS were collected. The ion conductivity (σ) was obtained from equation: $\sigma = L / (Z \times A)$, where the thickness of sample was showed by L (cm), sample area was represented by A (cm^2) and impedance was indicated by Z (Ω)$^{20-22}$. 1.0 M LiPF$_6$ liquid electrolyte (denoted as LiPF$_6$-LE)-filled TPB-DMTP-COF pellets laminated with stainless steels as inert electrodes. The resistance files: Nyquist plot of different separators with 1M LiPF$_6$-EC/DMC/EMC (1/1/1, by volume) electrolyte and pure liquid electrolyte (Fig. S8).

The typical impedance plots consist of a high-frequency semicircle followed by a low-frequency straight line, which corresponds to the bulk/grain boundary resistances and the diffusion of lithium ions, respectively. The absence of the semicircular portion disappears (Fig. S8f-j), indicating that the current carriers are ions and the total conductivity is the result of ionic conduction.[22-23] Thus, the model we used here only includes the resistance of ions diffusion, which was retrieved from the intercept of the straight line on the Z_{real} axis.[24] Meanwhile, in the case of the presence of high-frequency semicircle (Fig. S8a-e, Fig. S8k-o), the model contains boundary resistances and diffusion resistance was applied, and the ionic resistance was retrieved from the intercept of the extended straight line, which intersected with the semicircle.

The 1-10 sheets of Celgard2400 membranes filled with 1M $LiPF_6$ liquid electrolyte were measured resistance. The resistance files were plotted as a function of the number of membrane sheets, and the plot was found to be linear (Fig. S9, ESI†). Then, from the slope of the straight line passing through the origin, we estimated the ionic conductivity of $LiPF_6$-LE in the separator.

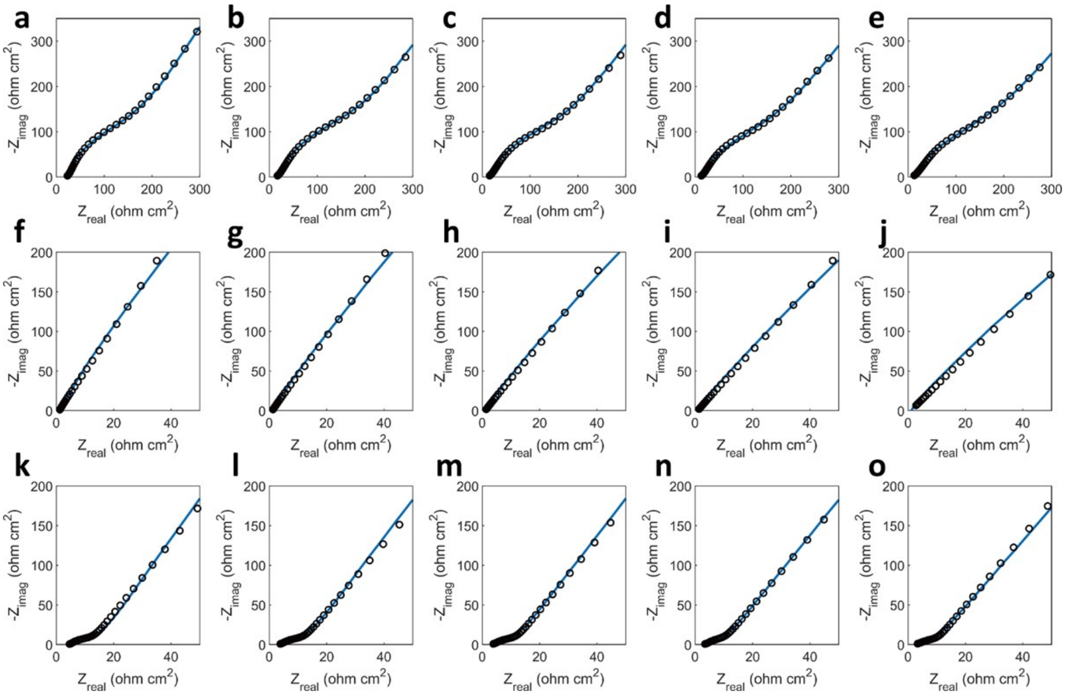

Fig. S8 Impedance spectroscopy. Nyquist plot of (**a-e**) 1M $LiPF_6$ in EC/DMC/EMC (1/1/1, by volume) electrolyte. (**f-j**) Celgard 2400 in 1M $LiPF_6$- EC/DMC/EMC electrolyte. (**k-o**) TPB-DMTP-COF in 1M $LiPF_6$- EC/DMC/EMC electrolyte measured at 20, 30, 40, 50, 60 °C, respectively.

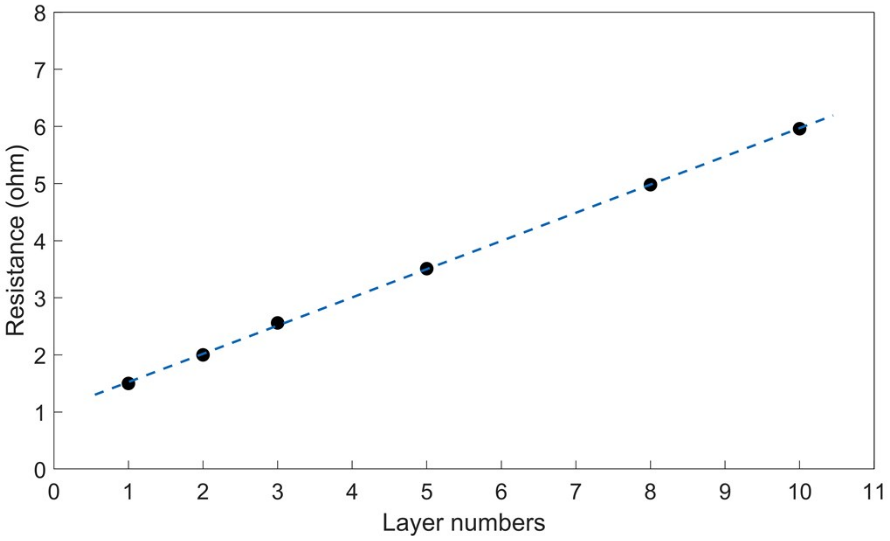

Fig. S9 Impedances of different layers of Celgard2400 in 1 M $LiPF_6$ in EC/DMC/EMC (1/1/1, by volume) electrolyte measured at 30 ^{o}C. **(**one layer, two layers, three layers, five layers, eight layers, ten layers).

F. SEM image of complex Celgard+TPB-DMTP-COF membrane and conductivity comparison of reported separators.

SEM image of complex Celgard+TPB-DMTP-COF membrane

The porosity of pristine Celgard was greatly reduced as most holes were filled with TPB-DMTP-COF particles (Fig. S10).

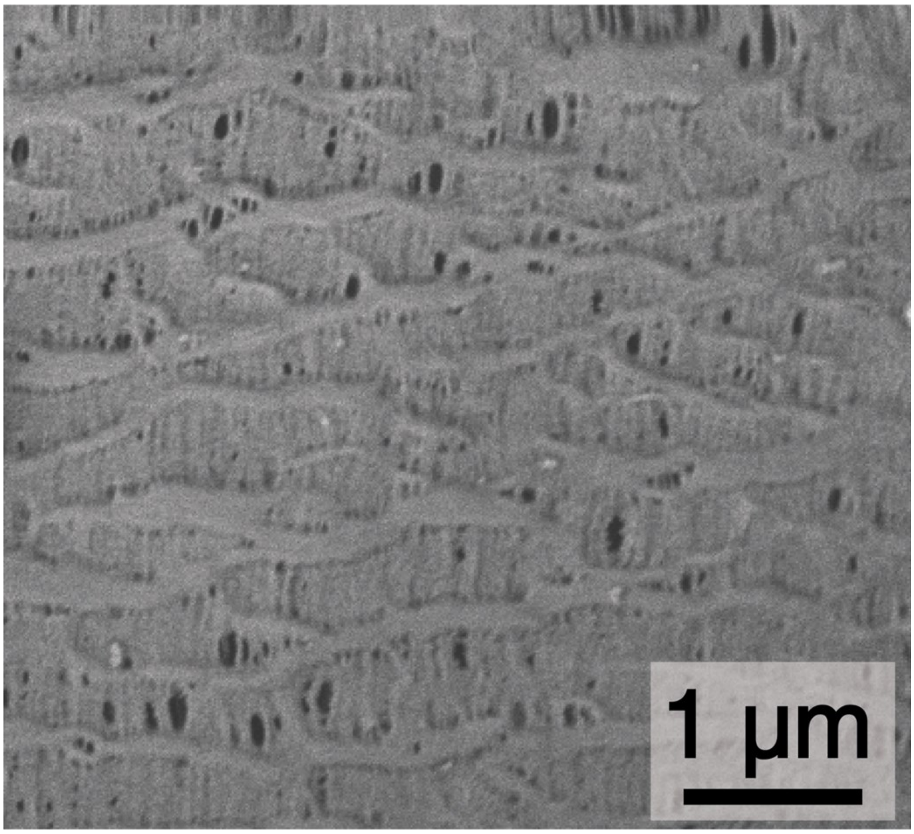

Fig. S10 SEM image of the complex Celgard+TPB-DMTP-COF membrane.

conductivity comparison of reported separators

$LiPF_6$-LE@COF had greater ionic conductivity than the reported membranes

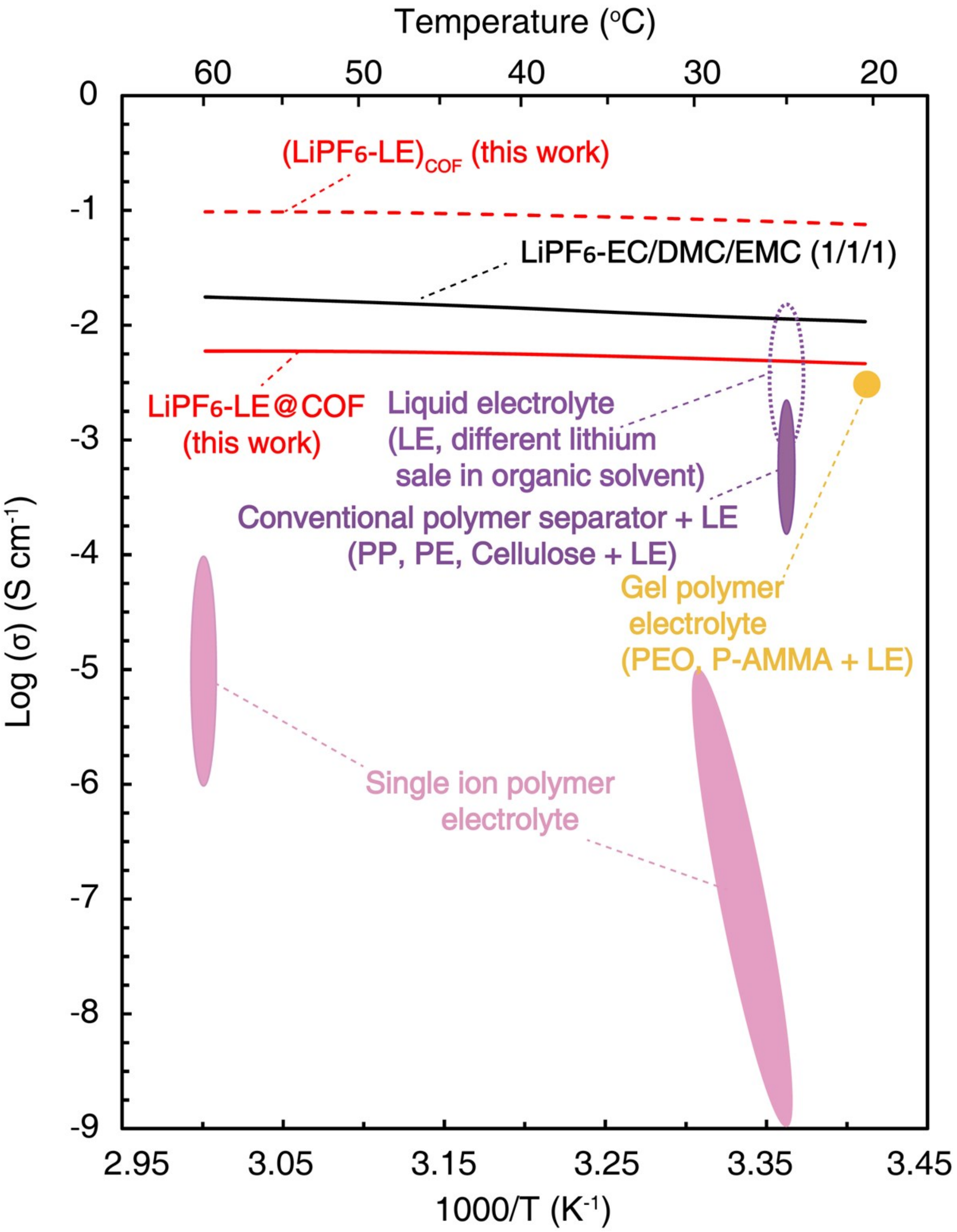

Fig. S11 Ionic conductivity of $LiPF_6$-LE@COF,and other lithium single ion polymer electrolyte, gel polymer electrolyte, conventional polymer separator in liquid electrolyte and liquid electrolyte.[20, 25-39]

G. Transference Number Measurements.

For transference number measurement, lithium electrodes are used to enable the reversibly exchange of lithium ions but block the anions.[40] The electrolyte-filled Celgard and COF in a lithium symmetric cell, which was assembled in an argon-filled glove box. Measurements were performed on a CHI660E Electrochemical Workstation (Shanghai Chenhua). When a constant dc bias (which should be low enough to obtain a linear response from the system; it was set as 10 mV in the present study) was applied to the electrodes of the electrolytic cell, the current fell from an initial value (i_0) to a steady-state value (i_∞), which was generally reached after several hours.

The symmetrical configuration of this cell is

$$\text{Li (metal)} \mid \text{separator} + \text{LiPF}_6\text{-EC/DMC/EMC electrolyte} \mid \text{Li (metal)} \quad (1)$$

The applied electric field difference in this two electrodes setup affects both ions in the same way. And in real cells which processes taking place at the electrode surface can be mainly ascribed to the charge transfer and the ionic conduction through the dynamic passivation layer, i.e. an intrinsic electrical resistance of the passive film, and t_{Li+} can be deduced from

$$t_{Li+} = \frac{i_\infty(\Delta V - i_0 R_0^{'})}{i_0(\Delta V - i_\infty R_\infty^{'})} \qquad (2)$$

In Equation S2, the subscripts 0 and ∞ indicate initial values and steady-state values, respectively, and R' is the sum of the charge transfer resistance R_{ct} and the passivating film resistance R_{film}; ΔV is the polarization voltage and i is the current; $R_0^{'}$ and $R_\infty^{'}$ can be achieved easily by recording two impedance spectra on the cell in the frequency range between 0.1 Hz and 10 KHz before the polarization, and after the steady-state has been reached and the dc bias potential has been removed. t_{Li+} of $LiPF_6$-LE@Celgard was measured to be 0.37 (Fig. S12), while for $LiPF_6$-LE@COF was 0.79 (Fig. S13), which showed a significantly improve t_{Li+}.

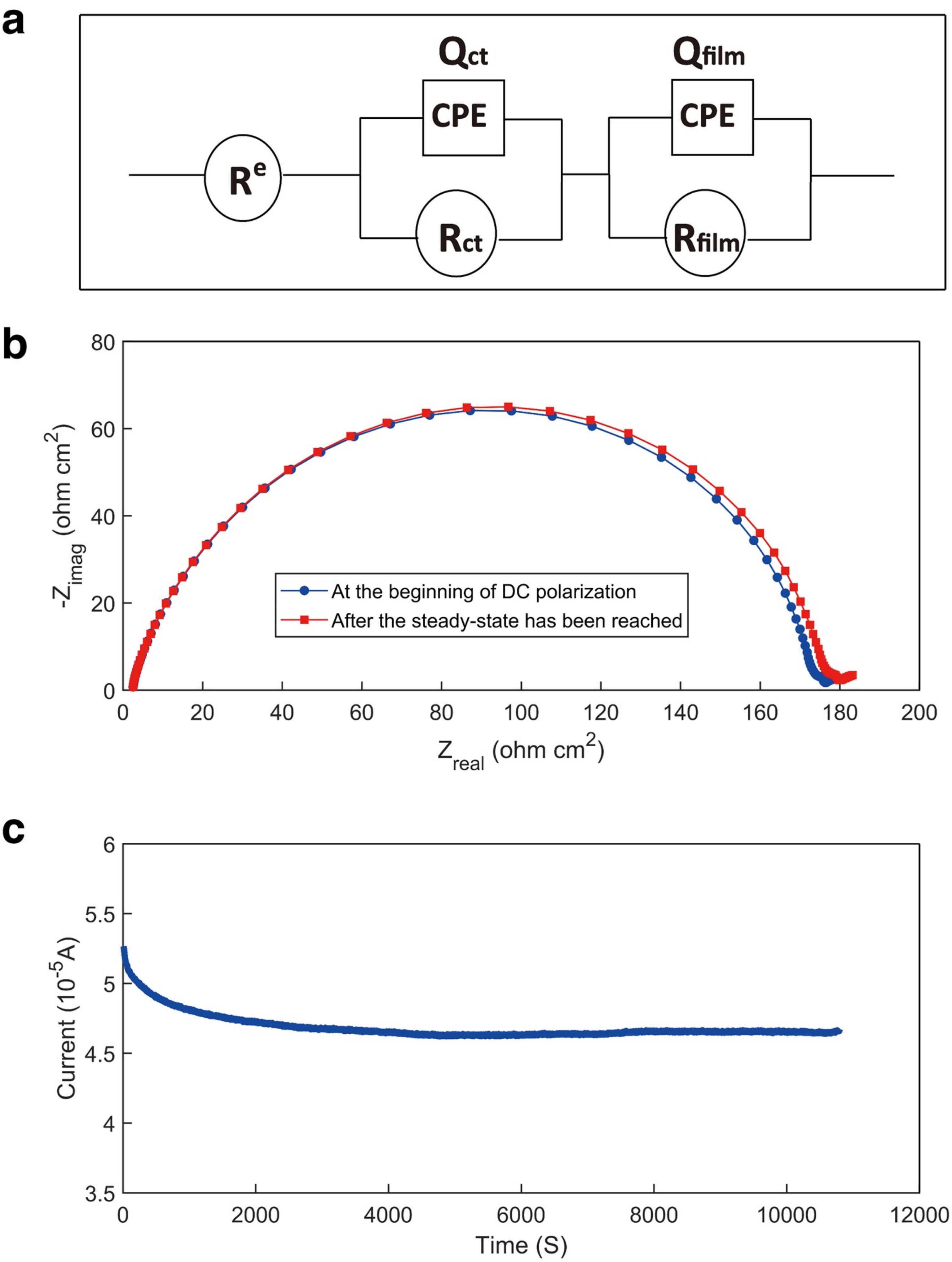

Fig. S12 (a) Equivalent circuit for deconvolution of the EIS spectra. (b) Impedance spectra of the cell with $LiPF_6$@celgard 2400 before polarization (blue curve), after the steady-state has been reached (red curve). (c) Polarization curve of the same cell.

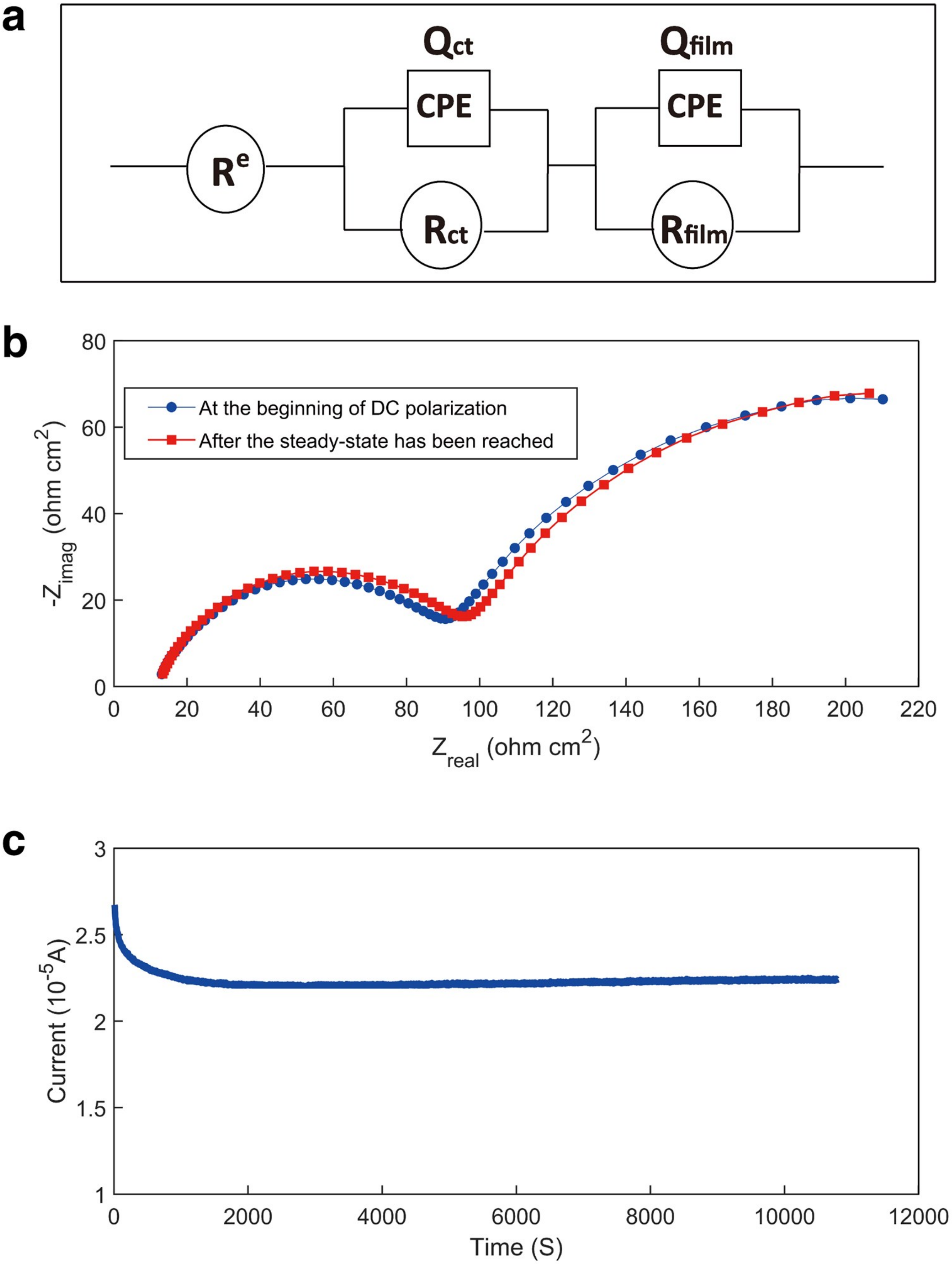

Fig. S13 (a) Equivalent circuit for deconvolution of the EIS spectra. (b) Impedance spectra of the cell with $LiPF_6$@COF before polarization (blue curve), after the steady-state has been reached (red curve). (c) Polarization curve of the same cell.

Table S4. Results of the electrochemical measurements.

Separator	i_0 (μA)	i_∞ (μA)	$R_0^{'}$ (Ω)	$R_\infty^{'}$ (Ω)	t_{Li+}
Celgard	5.27	4.66	177	180	0.37
TPB-DMTP-COF	2.67	2.22	92	97	0.79

H. Electrochemical stability

The electrochemical stability of the $LiPF_6$-LE@separator electrolytes was demonstrated in Fig. S14. In general, the electrochemical stability window is obtained using cyclic voltammograms, which was conducted on asymmetric cells, a stainless steel as the working electrode and a lithium metal disk as both the reference and counter electrodes (steel/$LiPF_6$-LE@seperator/Li). The testing was carried out by using CHI660E Electrochemical Workstation (Shanghai Chenhua) and recorded at a scan rate of 10 mV/s at room temperature using the $LiPF_6$-LE@Celgard and $LiPF_6$-LE@COF separators, respectively. The potential sweep was performed between -0.5 V and 4.5 V. As shown in Fig. S14, the COF with 1 M $LiPF_6$/(EC:DMC:EMC) (1:1:1, in volume solution have a wide electrochemical voltage window, which exhibited a stable plateau up to 4.5 V (versus Li^+/Li) without an irreversible oxidation. The behaviour was similar to that of the Celgard. This indicated that it is sufficiently high to serve as the most common lithium-ion electrodes because of no decomposition in this potential region.

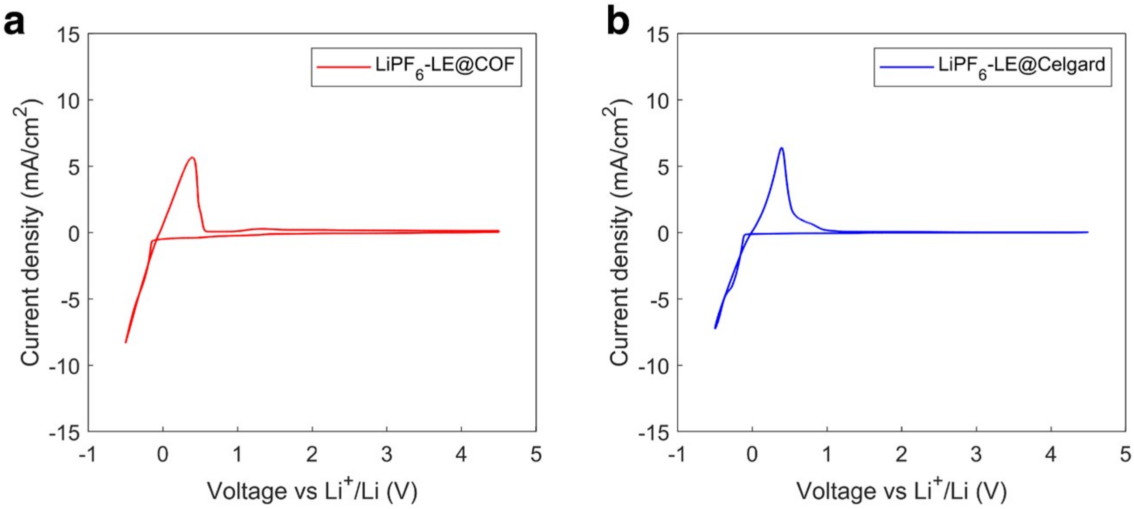

Fig. S14 Electrochemical stability of Celgard and TPB-DMTP-COF.Cyclic voltammograms (CVs) of (a) TPB-DMTP-COF and (b) Celgard 2400, respectively.

I. References.

1 A. V. Neimark, Y. Z. Lin, P. I. Ravikovitch and M. Thommes, *Carbon*, 2009, **47**, 1617.

2 A. M. Puziy, O. I. Poddubnaya, B. Gawdzik and M. Sobiesiak, *Adsorption*, 2015, **22**, 459.

3 N. Metropolis, A. W. Rosenbluth, M. N. Rosenbluth, A. H. Teller and E. Teller, *J. Chem. Phys.*, 1953, **21**, 1087.

4 H. Sun, *J. Phys. Chem. B*, 1998, **102**, 7338.

5 H. Sun, P. Ren and J. R. Fried, *Comput. Theor. Polym. Sci.*, 1998, **8**, 229.

6 H. Sun, Z. Jin, C. Yang, R. L. Akkermans, S. H. Robertson, N. A. Spenley, S. Miller and S. M. Todd, *J. Mol. Model.*, 2016, **22**, 47.

7 S. J. Clark, M. D. Segall, C. J. Pickard, P. J. Hasnip, M. J. Probert, K. Refson and M. C. Payne, *Z. Kristallogr.*, 2005, **220**, 567.

8 J. P. Perdew, K. Burke and M. Ernzerhof, *Phys. Rev. Lett.*, 1996, **77**, 3865.

9 S. Grimme, *J. Comput. Chem.*, 2004, **25**, 1463.

10 S. Grimme, *J. Comput. Chem.*, 2006, **27**, 1787.

11 J. Andzelm, C. Kolmel and A. Klamt, *J. Chem. Phys.*, 1995, **103**, 9312.

12 A. Klamt, V. Jonas, T. Burger and J. C. W. Lohrenz, *J. Phys. Chem. A*, 1998, **102**, 5074.

13 E. Mullins, R. Oldland, Y. A. Liu, S. Wang, S. I. Sandler, C. C. Chen, M. Zwolak and K. C. Seavey, *Ind. Eng. Chem. Res.*, 2006, **45**, 4389.

14 E. Mullins, Y. A. Liu, A. Ghaderi and S. D. Fast, *Ind. Eng. Chem. Res.*, 2008, **47**, 1707.

15 B. Delley, *J. Chem. Phys.*, 1990, **92**, 508.

16 B. Delley, *J. Phys. Chem.*, 2000, **113**, 7756.

17 P. Hohenberg and W. Kohn, *Phys. Rev. B*, 1964, **136**, B864.

18 W. Kohn and L. J. Sham, *Phys. Rev.*, 1965, **140**, 1133.

19 L. W. Finger, D. E. Cox and A. P. Jephcoat, *J. Appl. Crystallogr.*, 1994, **27**, 892.

20 Y. S. Zhu, S. Y. Xiao, Y. Shi, Y. Q. Yang, Y. Y. Hou and Y. P. Wu, *Adv. Energy Mater.*, 2014, **4**, 1300647.

21 Y. Hu, N. Dunlap, S. Wan, S. Lu, S. Huang, I. Sellinger, M. Ortiz, Y. Jin, S. H. Lee and W. Zhang, *J. Am. Chem. Soc.*, 2019, **141**, 7518.

22 M. Jacob, *Solid State Ionics*, 1997, **104**, 267.

23 J. Malathi, M. Kumaravadivel, G. M. Brahmanandhan, M. Hema, R. Baskaran and S. Selvasekarapandian, *J. Non-Cryst. Solids*, 2010, **356**, 2277.

24 S. Rajendran, O. Mahendran and R. Kannan, *Journal of Physics and Chemistry of Solids*, 2002, **63**, 303.

25 D. J. Bannister, G. R. Davies, I. M. Ward and J. E. Mcintyre, *Polymer*, 1984, **25**, 1291.

26 M. Watanabe, H. Tokuda and S. Muto, *Electrochim. Acta*, 2001, **46**, 1487.

27 S. W. Feng, D. Y. Shi, F. Liu, L. P. Zheng, J. Nie, W. F. Feng, X. J. Huang, M. Armand and Z. B. Zhou, *Electrochim. Acta*, 2013, **93**, 254.

28 H. Zhang, C. Li, M. Piszcz, E. Coya, T. Rojo, L. M. Rodriguez-Martinez, M. Armand and Z. Zhou, *Chem. Soc. Rev.*, 2017, **46**, 797.

29 S. S. Zhang, K. Xu and T. R. Jow, *Solid State Ionics*, 2003, **158**, 375.

30 S. S. Zhang, M. H. Ervin, K. Xu and T. R. Jow, *Solid State Ionics*, 2005, **176**, 41.

31 W. Y. Li, Y. Pang, J. Y. Liu, G. H. Liu, Y. G. Wang and Y. Y. Xia, *R. Soc. Chem. Adv.*, 2017, **7**, 23494.

32 D. Z. Wu, L. Deng, Y. Sun, K. S. Teh, C. Shi, Q. L. Tan, J. B. Zhao, D. H. Sun and L. W. Lin, *R. Soc. Chem. Adv.*, 2017, **7**, 24410.

33 M. Ue and S. Mori, *J. Electrochem. Soc.*, 1995, **142**, 2577.

34 W. Zhang, Z. Tu, J. Qian, S. Choudhury, L. A. Archer and Y. Lu, *Small*, 2018, **14**, e1703001.

35 C. W. Walker, J. D. Cox and M. Salomon, *J. Electrochem. Soc.*, 1996, **143**, L80.

36 L. A. Dominey, V. R. Koch and T. J. Blakley, *Electrochim. Acta*, 1992, **37**, 1551.

37 J. Barthel, R. Buestrich, E. Carl and H. J. Gores, *J. Electrochem. Soc.*, 1996, **143**, 3565.

38 J. Barthel, M. Wuhr, R. Buestrich and H. J. Gores, *J. Electrochem. Soc.*, 1995, **142**, 2527.

39 K. Xu, *Chem. Rev.*, 2004, **104**, 4303.

40 Y. C. Wen, X. S. Wang, Y. Yang, M. Z. Liu, W. Q. Tu, M. Q. Xu, G. Z. Sun, S. Kawaguchi, G. Z. Cao and W. S. Li, *J. Mater. Chem. A*, 2019, **7**, 26540.